

# Dilute quantum liquid in a K-Rb Bose mixture

V. Cikojević,<sup>1,2</sup> E. Poli,<sup>3,4</sup> F. Ancilotto,<sup>4</sup> L. Vranješ-Markić,<sup>1</sup> and J. Boronat<sup>2</sup>

<sup>1</sup>*University of Split, Faculty of Science, Rudera Boškovića 33, HR-21000 Split, Croatia*

<sup>2</sup>*Departament de Física, Universitat Politècnica de Catalunya, Campus Nord B4-B5, E-08034 Barcelona, Spain*

<sup>3</sup>*Institut für Experimentalphysik, Universität Innsbruck, Austria*

<sup>4</sup>*Dipartimento di Fisica e Astronomia "Galileo Galilei" and CNISM, Università di Padova, via Marzolo 8, 35122 Padova, Italy*

(Dated: July 14, 2021)

A quantum liquid in a heterogeneous mixture of <sup>41</sup>K and <sup>87</sup>Rb atoms is studied using the diffusion Monte Carlo method and Density Functional Theory. The perturbative Lee-Huang-Yang term for a heterogeneous mixture is verified and it is proved to be valid only near the gas-liquid transition. Based on the equations of state of the bulk mixture, calculated with diffusion Monte Carlo, extensions to Lee-Huang-Yang corrected mean-field energy functionals (MF+LHY) are presented. Using Density Functional Theory, a systematic comparison between different functionals is performed, focusing on the critical atom number, surface tension, surface width, Tolman length, and compressibility. These results are given as a function of the inter-species interaction strength, within the stability domain of the liquid mixture.

## I. INTRODUCTION

A new quantum state of matter has been predicted [1], and experimentally realized [2–4] recently in ultracold atomic gases, where a subtle interplay between inter-species attractive interactions and quantum fluctuations may result in the formation of self-bound, ultradilute droplets. Such liquid droplets are fundamentally different from those in classical or Helium fluids, where they arise instead from the interplay between the short-range repulsive and long-range attractive components of the interatomic potential [5]. The existence of self-bound ultra dilute quantum droplets, made of atoms of a binary mixture of Bose-Einstein condensates, was predicted by Petrov [1] and has been experimentally confirmed shortly later [2, 3]. These systems, whose peculiar properties are shared by other systems like dipolar Bose gases [6–8], are characterized by ultralow densities, orders of magnitude lower than that of the prototypical quantum liquid, i.e., liquid helium. Noticeably, quantum droplets exist at temperatures that are several orders of magnitude lower than the freezing points of classical liquids.

Mean-field analysis predicts that binary mixtures of Bose-Einstein condensates become unstable against collapse when the attractive inter-species interaction overcomes the repulsive contact potential between atoms [9]. However, in the ultradilute liquid phase the mean-field collapse is avoided if beyond-mean-field first-order perturbative corrections, in the form of the Lee Huang Yang energy functional [10, 11], are included. This correction is repulsive in nature, and thus stabilizes the system.

The formation of heteronuclear quantum droplets in an attractive bosonic mixture of <sup>41</sup>K and <sup>87</sup>Rb has been observed recently [4]. At variance with the largely studied mixture of two hyperfine states of <sup>39</sup>K, longer lived self-bound states are observed in the K-Rb mixture, both in free space and in optical waveguides. The K-Rb mixture has proven to be robust even when the two components are exposed to different confining potentials. Such long-

lived, self-bound droplets remain localized on a timescale of several tens of milliseconds, more than a factor of 10 larger than in the <sup>39</sup>K mixture [3].

The increased lifetime of this new liquid mixture allows not only for a more detailed experimental observation and characterization of isolated droplets, but will also permit the observation of more complex scenarios arising from the interactions between self-bound droplets. Moreover, the observed reduction of three-body losses allows for the realization of larger droplets. Recently, collisions between two droplets have been proposed as a useful experimental tool to investigate the dynamical properties of self-bound systems [12]. When two such droplets approach each other with a given relative velocity, they can either merge in a single droplet (coalescence) or separate into two or more droplets after the collision (bouncing/fragmentation) [13]. These different outcomes depend on whether or not the surface tension is large enough to counterbalance the kinetic energy of the colliding drops. A different phenomenology is expected for the coalescence dynamics of two droplets colliding at very small velocities, which, in analogy to previous studies on helium clusters, could be a probe of their superfluid properties. One interesting outcome of collision would be the formation of vortices or other topological structures during the merging process, as a consequence of their condensate nature. These effects are known to arise during the merging of superfluid liquid helium nanodroplets [14].

A fruitful comparison with experiments needs accurate and reliable theoretical schemes, which have not been applied yet on K-Rb mixture. The use of Density Functional Theory (DFT), in its time-dependent version, is known to allow a quite accurate description of the dynamics of inhomogeneous superfluid systems, even at the level of the Local Density approximation. Finite-range effects permit to widen the applicability of numerical simulations by going beyond the usual mean-field theory corrected with the LHY term (MF+LHY).

A most natural way to include such effects within the DFT scheme is to use density functionals built from results of first-principles quantum Monte Carlo calculations for the homogeneous phase [15, 16]. Importantly, first-principles finite- $N$  QMC calculations in the low-density regime show good agreement with the DFT approach [17] only in the vicinity of the gas-liquid transition while, at larger densities, modifications to MF+LHY approach are necessary [18–21].

This work is organized as follows. In Sec. II, we introduce the MF+LHY functional for a K-Rb mixture and predict a range of scattering lengths which allow self-bound state. In Sec. III, we describe the diffusion Monte Carlo (DMC) methodology for obtaining the ground-state energies of the bulk mixture. We report the DMC energies obtained using the short-range and finite-range potentials in Sec. IV and Sec. V, respectively. In Sec. VI, we apply the density-functional formalism to the characterization of the droplets, comparing the MF+LHY and QMC-based functionals for each quantity. Namely, we provide results for the surface tension, density profile, critical atom number, surface width, compressibility, and Tolman length for an experimentally relevant range of scattering parameters. Finally, a summary of results and conclusions is given in Sec. VII.

## II. MF + LHY EQUATION OF STATE

We consider a homogeneous, heteronuclear Bose-Bose mixture with two components (with masses  $m_1$  and  $m_2$ ) in a volume  $V$  and a total number of bosons  $N = N_1 + N_2$ . By neglecting finite-range effects (which will be considered in Sec. III), only the  $s$ -wave scattering lengths are used to characterize the inter-particle interactions. Within the LHY-extended mean-field framework (abbreviated MF+LHY hereafter), the energy of the system per unit volume is given by the functional [1]

$$\mathcal{E} = \mathcal{E}_{\text{MF}} + \mathcal{E}_{\text{LHY}} , \quad (1)$$

where the mean-field (MF) and Lee-Huang-Yang (LHY) terms read [9, 22, 23]

$$\mathcal{E}_{\text{MF}} = \frac{1}{2}g_{11}\rho_1^2 + \frac{1}{2}g_{22}\rho_2^2 + g_{12}\rho_1\rho_2 , \quad (2)$$

$$\mathcal{E}_{\text{LHY}} = \frac{8m_1^{3/2}(g_{11}\rho_1)^{5/2}}{15\pi^2\hbar^3} \left[ 1 + \left( \frac{m_2}{m_1} \right)^{3/5} \frac{g_{22}\rho_2}{g_{11}\rho_1} \right]^{5/2} , \quad (3)$$

Here,  $\rho_i$ , ( $i = 1, 2$ ) are the number densities of each component of the mixture, normalized such that  $\int_V \rho_i \, d\mathbf{r} = N_i$ , and  $g_{ij} = 2\pi\hbar^2 a_{ij}/\mu_{ij}$  are the  $ij$ -interaction strengths, with  $\mu_{ij}^{-1} = m_i^{-1} + m_j^{-1}$  the reduced mass.

The mixture of the two species is stable against fluctuations in the concentration  $N_1/N_2$  if [1]

$$\frac{\rho_2}{\rho_1} = \sqrt{\frac{g_{11}}{g_{22}}} . \quad (4)$$

As pointed out in Refs. [1, 22, 24], it is safe to assume that this optimal composition is realized everywhere in the system. Thus, the energy functional  $\mathcal{E}_{\text{MF+LHY}}[\rho] = \mathcal{E}_{\text{MF}}[\rho] + \mathcal{E}_{\text{LHY}}[\rho]$  becomes effectively single-component, and can be written in terms of the total density  $\rho = \rho_1 + \rho_2$ . Under this assumption, the MF and LHY terms read

$$\begin{aligned} \mathcal{E}_{\text{MF}} &= \frac{2\pi\hbar^2 \left( 2a_{11}m_2 + a_{12}\sqrt{\frac{a_{11}m_2}{a_{22}m_1}}(m_1 + m_2) \right)}{m_1m_2 \left( \sqrt{\frac{a_{11}m_2}{a_{22}m_1}} + 1 \right)^2} \rho^2 \quad (5) \\ \mathcal{E}_{\text{LHY}} &= \frac{256\sqrt{\pi}\hbar^2 a_{11}^{5/2}}{15m_1} \\ &\quad \times \left[ \frac{1 + \left( \frac{m_2}{m_1} \right)^{1/10} \sqrt{a_{22}/a_{11}}}{1 + \sqrt{\frac{m_2 a_{11}}{m_1 a_{22}}}} \right]^{5/2} \rho^{5/2} \quad (6) \end{aligned}$$

The MF+LHY energy per particle can be compactly written as

$$\frac{E/N}{|E_0^{\text{MF+LHY}}|/N} = -3 \frac{\rho}{\rho_0^{\text{MF+LHY}}} + 2 \left( \frac{\rho}{\rho_0^{\text{MF+LHY}}} \right)^{3/2} , \quad (7)$$

$\rho_0^{\text{MF+LHY}}$  being the equilibrium density within the MF+LHY theory, i.e., the density that minimizes the functional  $\mathcal{E}_{\text{MF+LHY}}[\rho]$ . Explicitly,

$$\begin{aligned} \rho_0^{\text{MF+LHY}} &= \frac{25\pi m_2^3 \left( 2a_{11}m_2 + a_{12}\sqrt{\frac{a_{11}m_2}{a_{22}m_1}}(m_1 + m_2) \right)^2}{4096 \left( a_{11}m_2 + a_{22}m_1 \left( \frac{m_2}{m_1} \right)^{3/5} \sqrt{\frac{a_{11}m_2}{a_{22}m_1}} \right)^5} \\ &\quad \times \left( \sqrt{\frac{a_{11}m_2}{a_{22}m_1}} + 1 \right) . \quad (8) \end{aligned}$$

The energy per particle at equilibrium is  $E_0^{\text{MF+LHY}}/N = \mathcal{E}_{\text{MF+LHY}}[\rho_0^{\text{MF+LHY}}]/\rho_0^{\text{MF+LHY}}$ . The fact that the MF+LHY functional can be written in a universal form (Eq. 7) proves that all the results from Ref. [1] can be applied here with a proper change of units.

In what follows, we define the hyperfine state  $|F = 1, m_F = 1\rangle$  of  $^{41}\text{K}$  as component 1, and the hyperfine state  $|F = 1, m_F = 1\rangle$  of  $^{87}\text{Rb}$  as component 2. The scattering parameters describing the intra-species repulsion are fixed and their values are equal to  $a_{11} = 65a_0$  [25] and  $a_{22} = 100.4a_0$  [26]. With those two parameters, the MF+LHY theory predicts a self-bound state (hereafter called "liquid") for  $a_{12} < a_{12}^c$ , with  $a_{12}^c$  given by

$$a_{12}^c = \frac{-2\sqrt{a_{22}/a_{11}}}{\sqrt{m_2/m_1}(1 + m_1/m_2)} \approx -75.4a_0 . \quad (9)$$

In the experiment, accessible values of  $a_{12}$  are in the range between  $a_{12} = -80a_0$  and  $a_{12} = -95a_0$  [4].

### III. DIFFUSION MONTE CARLO

We use the diffusion Monte Carlo (DMC) method to determine the energy per particle in the homogeneous phase. This method was previously applied in related problems regarding the study of a Bose-Bose liquid by some of the authors [15, 27]. DMC is nowadays a well-know method that is able to solve exactly the imaginary-time Schrödinger equation of the many-particle system, within some statistical noise. The starting point of DMC is the decomposition of the imaginary-time evolution operator. In this paper, we use a propagator that is accurate up to second order in the timestep [28], following the implementation outlined in Ref. [29].

To reduce the variance in the estimation of energy, we use standard importance sampling through a trial wavefunction, written as a Jastrow product over pairs [30]

$$\Psi(\mathbf{R}) = \prod_{j>i=0}^{N_1} f^{(11)}(r_{ij}) \prod_{j>i=N_1}^{N_1+N_2} f^{(22)}(r_{ij}) \prod_{i,j}^{N_1,N_2} f^{(12)}(r_{ij}), \quad (10)$$

where the two-particle correlation functions  $f^{(\alpha,\beta)}(r)$  ( $\alpha, \beta = 1, 2$ ) are chosen as

$$f^{(\alpha,\beta)}(r) = \begin{cases} f_{2b}(r) & r < \tilde{R} \\ B(1 - \frac{a_{\alpha,\beta}}{r}) & r < R_v, \\ C \exp(-\frac{D}{r} + \frac{E}{r^2}), & R_v < r < L/2 \\ 1, & r > L/2. \end{cases} \quad (11)$$

The two-particle correlation function at short distances  $f_{2b}(r)$  is the solution to the two-body problem for a given interaction potential. Throughout the paper we use short-ranged potentials, such that the potential is zero at distances greater than  $\tilde{R}$ . The function  $f_{2b}$  is connected to the asymptotic form  $1 - a_{\alpha,\beta}/r$ , where  $a_{\alpha,\beta}$  is a corresponding scattering length. At  $r = R_v$ , this is connected to the long-range phononic form  $C \exp(-\frac{D}{r} + \frac{E}{r^2})$  [31]. Finally, we impose that the function is constant (one) at the boundary of the simulation box ( $r = L/2$ ). This trial wavefunction has only one variational parameter, namely  $R_v$ , which we optimize variationally finding that, in all cases,  $R_v = 0.45L$ . Our DMC results are unbiased for time-steps  $\Delta\tau \lesssim 0.5m_{41}a_{11}^2/\hbar^2$  and walker number  $n_w \approx 200$ . Simulations are performed in a cubic box of size  $L = (N/\rho)^{1/3}$ , with periodic boundary conditions applied to particle coordinates. For each density, a set of several calculations of increasing number of particles, namely  $N = 130, 160, 200, 250$ , and  $500$  is performed in order to study finite-size effects. The final energies, corresponding to the thermodynamic limit, are obtained by an extrapolation to  $N \rightarrow \infty$  assuming a correction which decreases as  $N^{-1}$ .

### IV. SHORT-RANGE POTENTIALS

In a first approach to the problem, we use in DMC interatomic potentials that have a very short range, which

we call POT-SR in the following. Since we cannot use a contact interaction in DMC, we model the short-range interaction by a set of potentials with a range  $r_p$  satisfying  $\rho r_p^3 \ll 1$ , where  $\rho$  is the typical number density. Under this criterium, we choose a hard-core potential for repulsive interactions (between equal species), with a diameter corresponding to the  $s$ -wave scattering length [9]

$$V_{ii}(r) = \begin{cases} \infty & r < a_{ii}, \\ 0, & \text{otherwise} \end{cases}, \quad i = 1, 2. \quad (12)$$

The attraction between different species is modeled by a short-range square-well potential,

$$V_{12}(r) = \begin{cases} -V_{sr}, & r < R_{sr}, \\ 0, & \text{otherwise} \end{cases}, \quad (13)$$

where we choose  $R_{sr} = a_{11}$ . The particular choice of potentials given in Eqs. (12) and (13) resembles a zero-range case, since the probability of finding two particles within the diameter  $R_{sr}$  is  $\rho_0 R_{sr}^3 \approx 2 \cdot 10^{-4}$ , evaluated at the equilibrium density for the densest liquid analyzed, corresponding to  $a_{12} = -95a_0$ . By properly setting  $V_{sr}$ , we obtain a target scattering length  $a_{12}$ , which for a square-well potential is given by [32]

$$a_{12} = R_{sr} \left\{ 1 + \frac{\tan(K_0 R_{sr})}{K_0 R_{sr}} \right\}, \quad (14)$$

where  $K_0 = \sqrt{2V_{sr}(m_1 + m_2)/(\hbar^2 m_1 m_2)}$ . DMC results of the energy per particle, obtained with POT-SR potentials (Eqs. 12 and 13), are shown in Fig. 1, for  $a_{12} = -77a_0, -85a_0, -90a_0$ , and  $-95a_0$ , which include experimentally accessible values. They are compared with the predictions of MF +LHY theory. The DMC energy per particle is well fitted to the form

$$\frac{E}{N} = \alpha\rho + \beta\rho^\gamma, \quad (15)$$

where  $\alpha, \beta$ , and  $\gamma$  are the fitting parameters. The equilibrium density and the coefficients of the fit to the DMC energy per particle are reported in Table I. As we can see in Fig. 1, the DMC results of the energy per particle reproduce well the MF +LHY theory for  $a_{12} = -77a_0$ , which is close to the critical value,  $a_{12}^c = -75.4a_0$ . However, the DMC results for different  $a_{12}$  do not fit a single line defined by Eq. (7), implying that the universality of the MF +LHY theory is broken, with the deviation growing as  $a_{12}$  becomes larger. Interestingly, we observe repulsive beyond-LHY contributions when the fluid enters a more correlated regime. Repulsive beyond-LHY contributions to the energy have already been observed in symmetric Bose-Bose fluids [27] and in the liquid  $^{39}\text{K}$  mixture [15] for the potentials with a small effective range. This effect could be due to bosonic pairing between atoms of different species [19, 20].

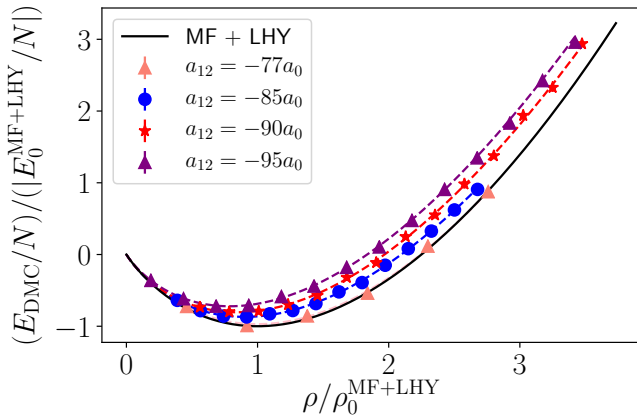


FIG. 1. DMC energy per particle as a function of density, obtained with the POT-SR models (Eqs. 12 and 13), in a mixture having the optimal composition  $\rho_2/\rho_1 = \sqrt{g_{11}/g_{22}}$ . Energy per particle and the total density are normalized with respect to the equilibrium values given in Eq. (8).

TABLE I. Coefficients of fit  $E/N = \alpha\rho a_{11}^3 + \beta(\rho a_{11}^3)^\gamma$  of the DMC energies per particle, obtained with short-range set of potentials POT-SR (Eqs. (12) and (13), reported in Fig. (1). Parameters  $\alpha$  and  $\beta$  are given in units  $\hbar^2/(m_1 a_{11}^2) = 10^{-3}$  Kelvin, and  $\gamma$  is adimensional.  $\rho_0$  stands for the equilibrium density of a QMC functional. Scattering lengths in the repulsive channel are  $a_{11} = 65a_0$  and  $a_{22} = 100.4a_0$ .

$a_{12}$	Method	$\alpha$	$\beta$	$\gamma$	$\rho_0 a_{11}^3$
$-77a_0$	QMC	-0.056	35.709	1.500	$1.08 \times 10^{-6}$
	MF+LHY	-0.057	36.437	1.5	$1.09 \times 10^{-6}$
$-85a_0$	QMC	-0.385	15.981	1.395	$3.48 \times 10^{-5}$
	MF+LHY	-0.340	36.437	1.5	$3.86 \times 10^{-5}$
$-90a_0$	QMC	-0.592	16.344	1.384	$7.53 \times 10^{-5}$
	MF+LHY	-0.516	36.437	1.5	$8.92 \times 10^{-4}$
$-95a_0$	QMC	-0.772	16.768	1.379	$1.26 \times 10^{-4}$
	MF+LHY	-0.693	36.437	1.5	$1.61 \times 10^{-4}$

## V. FINITE-RANGE POTENTIALS

The effective range in the  $^{41}\text{K}$ - $^{87}\text{Rb}$  mixture is not known, but can be estimated from the combined knowledge of the  $C_6$  coefficient of the leading term in the long-range tail of the Van Der Waals interaction potential and the scattering length obtained from measurements of the Feshbach resonances [33–35]. Knowing the van der Waals coefficient  $C_6$ , one can estimate the effective range using a semiclassical approximation [35],

$$r_{\text{eff}} = \frac{\Gamma(1/4)^2}{6\pi} a_m \left( 1 - 2\frac{a_m}{a} + 2\left(\frac{a_m}{a}\right)^2 \right), \quad (16)$$

with  $a_m = 4\pi R_{\text{vdw}}/\Gamma(1/4)^2$  the mean scattering length and  $R_{\text{vdw}} = (2\mu C_6/\hbar^2)^{1/4}/2$  the van der Waals length,

TABLE II.  $C_6$  coefficients of each channel and the corresponding scattering lengths and effective ranges.

Channel	$C_6$ (a. u.)	$a/a_0$	$r_{\text{eff}}/a_0$
K-K (1-1) [25, 37]	3897	65	168
Rb-Rb (2-2) [26]	4707	100.4	153
K-Rb (1-2) [38]	4285	-85	795
		-90	748
		-95	707

where  $\mu$  is the reduced mass. The  $C_6$  coefficients for  $^{41}\text{K}$  and  $^{87}\text{Rb}$  are given, along with the effective ranges derived from (16), in Table II.

Since only two scattering parameters, namely the scattering length  $a$  and the effective range  $r_{\text{eff}}$ , cannot uniquely define the interaction potential, we resort to model potentials satisfying the two scattering criteria. To investigate the role of the "shape" of the interaction dictated by the higher-order scattering parameters, we performed two independent sets of calculations, each having different models of the interaction potential. We call the two models POT-I and POT-II, and both can be written as follows

$$V(r) = \begin{cases} V_0 & 0 < r < R_0, \\ -V_1, & R_0 < r < R_1, \\ 0, & \text{otherwise.} \end{cases} \quad i = 1, 2. \quad (17)$$

This particular form of interaction is convenient because the analytic expressions for both the  $s$ -wave scattering length and effective range are analytically known [36]. The specific values of the interaction parameters in all three channels for POT-I and POT-II potentials are summarized in Table III.

In Fig. (2), we report the comparison between the DMC and MF+LHY equations of state, for three values of  $a_{12}$  and using POT-I and POT-II as model potentials (see Eq. (17) and Table (III)). For all three values of  $a_{12}$ , there is a slight increase in the equilibrium density, relative to the MF+LHY theory. This phenomenon was previously observed in a mixture with symmetric interactions [17, 18, 27], whereas in a  $^{39}\text{K}$  liquid mixture [15] the significant increase of equilibrium density occurs because in that mixture the effective range is much larger than in the K-Rb one. In other words, in the K mixture the finite-range, beyond-LHY, negative energy contributions dominate. On the other hand, we observe that energies obtained with two different potentials but with the same  $s$ -wave scattering length and effective range collapses to a single equation of state, at least at densities not much larger than the equilibrium one. Therefore, the range of universality is extended, but now in terms of two scattering parameters [15].

## VI. DENSITY-FUNCTIONAL RESULTS

The stability of the self-bound mixture of  $^{41}\text{K}$ - $^{87}\text{Rb}$  in free space implies the presence of a surface and a positive

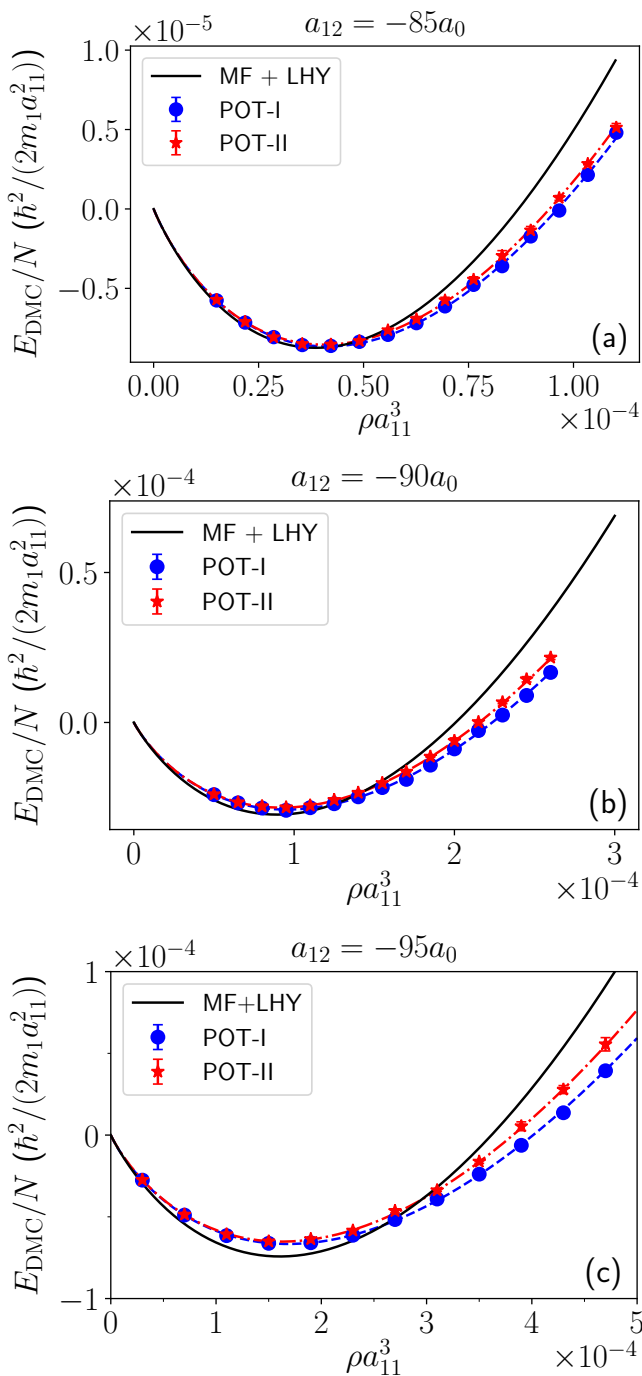


FIG. 2. Energy per particle as a function of density, for values of  $a_{12} = -85a_0$  (a),  $a_{12} = -90a_0$  (b) and  $a_{12} = -95a_0$  (c). DMC calculations are performed with POT-I and POT-II potentials, which satisfy both scattering parameters (see Eq. (17) and table (IV)). Ratio of concentrations  $\rho_2/\rho_1 = \sqrt{g_{11}/g_{22}}$  is kept fixed for each density, a criteria coming from the mean-field, also verified by QMC to predict the ground state.

TABLE III. Parameters of POT-I and POT-II potentials which reproduce both scattering parameters (see Table II).  $R_0$  and  $R_1$  are given in units  $a_{11} = 65a_0$ , and  $V_0$  and  $V_1$  are given in units  $\hbar^2/(m_1a_{11}^2) = 10^{-3}$  Kelvin.

$a$	Legend	$R_0$	$R_1$	$V_0$	$V_1$
$65a_0$	POT-I	1.8797	0	1.2123	0
	POT-II	2.8386	3.5581	0.9140	0.3687
$100.4a_0$	POT-I	2.7084	0	0.3337	0
	POT-II	3.8374	4.8201	0.2366	0.0824
$-85a_0$	POT-I	0	4.8897	0	0.01865
	POT-II	2.7513	3.6684	0.0632	0.1189
$-90a_0$	POT-I	0	4.8069	0	0.0205
	POT-II	2.7419	3.6558	0.0586	0.1197
$-95a_0$	POT-I	0	4.7315	0	0.0222
	POT-II	2.7329	3.6438	0.0541	0.1205

TABLE IV. Coefficients of fit  $E/N = \alpha\rho a_{11}^3 + \beta(\rho a_{11}^3)^\gamma$  of the DMC energies per particle, obtained with set of potentials POT-I and POT-II (see Eq. (17) and Table (III)). Comparison between different functionals are presented in Fig. (2). Parameters  $\alpha$  and  $\beta$  are given in units  $\hbar^2/(m_1a_{11}^2) = 10^{-3}$  Kelvin, and  $\gamma$  is adimensional. Scattering lengths in the repulsive channel are  $a_{11} = 65a_0$  and  $a_{22} = 100.4a_0$ . For comparison, MF+LHY parameters are written in Table (I).

$a_{12}$	Potentials	$\alpha$	$\beta$	$\gamma$
-85	POT-I	-0.37	14.087	1.393
	POT-II	-0.371	14.547	1.396
-90	POT-I	-0.578	11.778	1.359
	POT-II	-0.573	12.894	1.369
-95	POT-I	-0.824	9.752	1.316
	POT-II	-0.774	12.22	1.351

surface tension associated to it. We studied the surface properties of spherical  $^{41}\text{K}$ - $^{87}\text{Rb}$  droplets within the DFT approach in the MF+LHY framework, for a fixed ratio of densities  $\rho_2/\rho_1 = \sqrt{g_{11}/g_{22}}$  corresponding to the equilibrium one for the homogeneous mixture. We provide additional results using a more accurate density functional obtained from the ab-initio QMC results discussed in the previous Section.

We have first studied a planar surface, with the aim of determining the surface tension  $\sigma$  in a range of values of the inter-particle attractive interaction  $a_{12}$  accessible to the experiments. When studying a planar surface, it is useful to use a slab geometry, i.e., we assume an extended homogeneous system in the  $xy$  plane (with periodic boundary conditions), and with a finite extension along the  $z$ -direction. In this direction, two liquid-vacuum interfaces are formed, with the slab width thick enough to have a constant density region between the two confining surfaces ("bulk" phase). This amounts to neglect curvature effects, which will be explicitly considered later on. The surface width of the density profile along

$z$  can be quantified by the parameter  $\Delta$ , which measures the width between surface points at 90% and 10% of the bulk total density.

By defining the following coefficients,

$$C_K = \frac{1}{4} \left( \frac{\hbar^2}{2m_1} + \frac{\hbar^2}{2m_2} \sqrt{\frac{g_{11}}{g_{22}}} \right), \quad (18)$$

$$C_\delta = g_{11} + g_{12} \sqrt{\frac{g_{11}}{g_{22}}}, \quad (19)$$

$$C_\rho = \frac{8}{15\pi^2} \left( \frac{m_1}{\hbar^2} \right)^{3/2} g_{11}^{5/2} \left[ 1 + \left( \frac{m_1}{m_2} \right)^{3/5} \sqrt{\frac{g_{22}}{g_{11}}} \right], \quad (20)$$

the effective single-component energy density of the mixture within the MF+LHY theory, expressed for simplicity in terms of the density  $\rho_1$ , reads

$$\mathcal{E} = C_K \frac{(\nabla \rho_1)^2}{\rho_1} + C_\delta \rho_1^2 + C_\rho \rho_1^{5/2}. \quad (21)$$

We recall that knowledge of one density is enough to characterize the whole droplet because of the underlying assumption  $\rho_2/\rho_1 = \sqrt{g_{11}/g_{22}}$  [22, 24].

Remarkably, the surface tension of the planar interface described by local energy functionals of the form (21) can be estimated, without any prior knowledge of the density profile, by calculating the following integral [39],

$$\sigma = 2 \int_0^{\rho_0} d\rho_1 \sqrt{C_K (C_\delta \rho_1 + C_\rho \rho_1^{3/2} - \mu_0)}, \quad (22)$$

where  $\mu_0 = C_\delta \rho_1 + C_\rho \rho_1^{3/2}$  is the chemical potential of a liquid system in equilibrium with the vacuum, evaluated at the equilibrium density  $\rho_0$ . The density profile can also be obtained by simple quadrature, solving the implicit equation

$$z(\rho) = z_0 + \int_{\rho_0/2}^{\rho} \frac{1}{h(\rho')} d\rho' \quad (23)$$

where  $\rho(z_0) = \rho_0/2$  and

$$h(\rho) = -\sqrt{\left( \frac{\rho}{C_K} \right) [C_\delta \rho^2 + C_\rho \rho^{5/2} - \mu_0 \rho]} \quad (24)$$

Here  $\rho$  can have any value in the interval  $[0, \rho_0]$ .

The calculated surface tension for different values of  $a_{12}$  is shown in Fig. 3, and compared with the results obtained from the QMC-based functional. Notice that relatively small changes in the inter-species interaction strength cause order-of-magnitude changes in the surface tension, which is highlighted by the logarithmic scale introduced in the  $\sigma$ -axis. Surface tension obtained with the QMC-based functionals POT-SR and POT-I are both below the predictions of the MF+LHY functional, with POT-SR having larger deviations from MF+LHY.

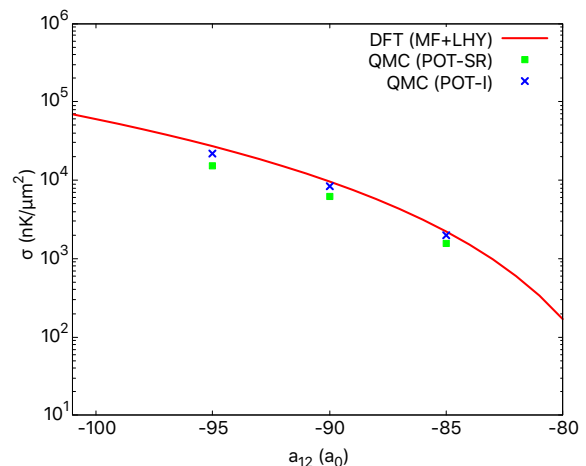


FIG. 3. Surface tension as a function of the (attractive) inter-species scattering length  $a_{12}$ . The solid red line is obtained using the MF+LHY functional, green squares and blue crosses are the predictions assuming POT-SR and POT-I functionals, respectively (see Table I and IV).

The width of the liquid-vacuum interface profile is strongly dependent on the inter-species scattering length  $a_{12}$ . In a droplet this will affect the overall shape of the droplet itself, depending upon the value of the total number of particles  $N$ . For larger values of  $N$  the droplet will be characterized by a central region of fairly uniform density (“bulk”) and an external surface region where the density drops to zero with the distance from its center, whereas it will be an “all surface”, gaussian-like droplet, where the central bulk region is almost absent, for low values of  $N$ . By defining the droplet radius  $R$  as

$$R = \sqrt[3]{\frac{3N}{4\pi\rho_{\text{bulk}}}}, \quad (25)$$

in the first case the ratio between the surface width  $\Delta$  and the droplet radius  $R$  is  $\Delta/R \ll 1$ , while in the second case  $\Delta/R \gg 1$ .

We must notice that not all values of  $N$  are allowed in a droplet for a given  $a_{12}$  because small droplets, i.e., those with a number of particles below some critical value  $N_c$  become unstable when the kinetic energy dominates over the interaction energy, eventually causing the evaporation of the droplet. In order to estimate the critical size  $N_c$  we make a simple variational ansatz for the radial density profile, which is a good approximation for spherical, small droplets:

$$\rho_1(r) = \frac{N_1}{\pi^{3/2}\sigma^3} e^{-r^2/\sigma^2}. \quad (26)$$

We use the above ansatz in the energy functional (21) and impose the condition for a minimum,  $\partial E/\partial\sigma = 0$ , together with the additional requirement  $E = 0$  which marks the line separating stable droplets with negative



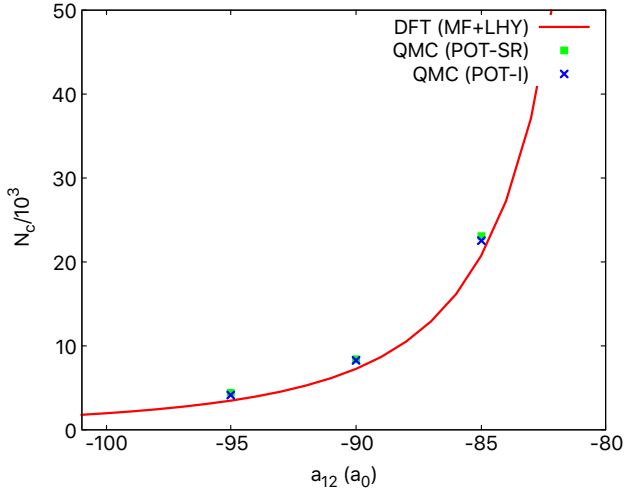


FIG. 4. Critical atom number  $N_c$  as a function of the interspecies scattering length. The solid red line is obtained using the MF+LHY functional, green squares and blue crosses are the predictions assuming POT-SR and POT-I functionals, respectively (see Table I and IV).

total energies from unstable ones with positive energies. Solving for the total number of atoms of species 1,  $N_1$ , we find the critical droplet size  $N_c = N_{c1}(1 + \sqrt{g_{11}/g_{22}})$ , where

$$N_{c1} = -\frac{c}{\lambda^{9/2}(a/\lambda^2 + b/\lambda^3)} \quad (27)$$

Here  $\lambda = -3b/5a$ , with  $a, b, c$  being given by the expressions  $a = 6C_K$ ,  $b = C_\delta/(2\pi^{3/2})$  and  $c = 4C_\rho/(5\sqrt{10}\pi^{9/4})$ . The table V and the figure 4 show the critical atom number for some values of the scattering length computed with DFT and QMC methods.

Figure 5 summarizes our results: the color scales shows the ratio between the surface width  $\Delta$  and the radius  $R$  of the droplet, which evaporates for a number of particles below the critical value (solid black line). The red region identifies gaussian-like, "all-surface" droplets, while the green and blue region identifies droplets with a well defined, central "bulk" density. Notice that the black line belongs to the red region for each  $|a_{12}|$  so the assumption of a gaussian density profile for the variational study of the critical atom number is indeed justified.

The surface tension for the  $^{41}\text{K} - ^{87}\text{Rb}$  self-bound mixture has been obtained for a planar interface (we will call it  $\sigma_0$  to distinguish it from the size-dependent surface tension of a droplet), though in real droplets an interfacial curvature of the surface in contact with the vacuum is present. The curvature-dependent surface tension can be expressed in term of the so-called Tolman length  $\delta$  [40]. To a first approximation the Tolman length  $\delta$  is independent of the droplet size, and it gives the size-dependent surface tension in term of the one for a planar surface

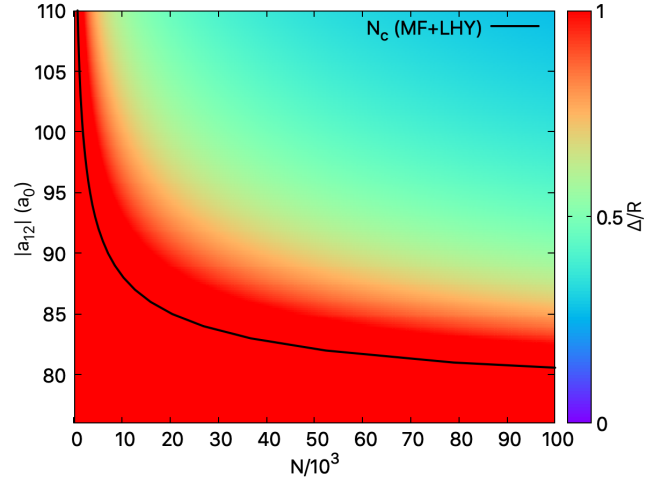


FIG. 5. The ratio  $\Delta/R$  is represented as a function of  $|a_{12}|$  and  $N$ . The red region identifies gaussian-like radial density profiles while the green and blue region identifies droplets with a central bulk region. The black solid line marks the total critical number of particles  $N_c$  below which the droplet evaporates.

[41, 42]

$$\sigma(R) = \sigma_0 \left(1 - \frac{2\delta}{R}\right). \quad (28)$$

A thermodynamic argument relates the Tolman length to the isothermal compressibility  $\kappa^{-1}$  and surface tension  $\sigma_0$  [43]

$$\delta \approx -\kappa^{-1}\sigma_0. \quad (29)$$

The isothermal compressibility  $\kappa^{-1}$  of a self-bound quantum mixture with equilibrium bulk densities  $\rho_1$  and  $\rho_2$  in the MF+LHY approach is given by [22]

$$\kappa^{-1} = \left(g_{11}\rho_1^2 + g_{22}\rho_2^2 + 2g_{12}\rho_1\rho_2 + \frac{15}{4}\mathcal{E}_{\text{LHY}}\right)^{-1}. \quad (30)$$

Previously, some studies have noticed that the product  $\kappa^{-1}\sigma_0$  is a fundamental characteristic length in liquid droplets [44–48] though the connection with the Tolman length  $\delta$  was never explicitly made. We checked the validity of Eq. (29) by independently computing  $\delta$  using the Liquid Drop Model (LDM), i.e., writing the calculated total energy of a droplet made of  $N$  atoms as

$$E = aN + bN^{2/3} + cN^{1/3} \quad (31)$$

where the separate bulk, surface and curvature contributions to the total energy of the droplet are highlighted. By using the relation (28) one can see that  $c = 8\pi(3/4\pi\rho_0)^{1/3}\sigma_0\delta$ . The coefficient  $c$  is in turn obtained by fitting the calculated energies using the LDM expression quoted above, allowing to determine the Tolman length  $\delta$ . Predictions for the Tolman length are summarized in Table V.

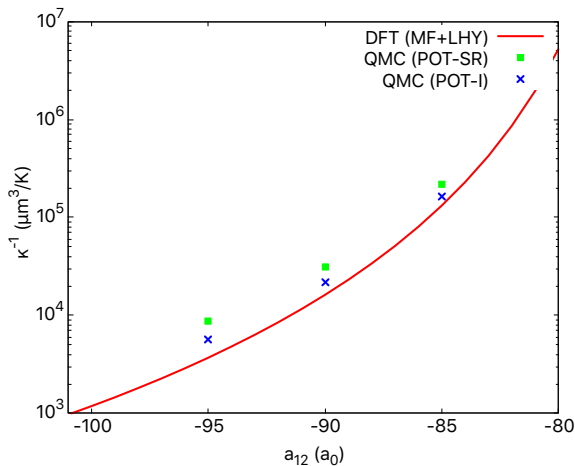


FIG. 6. Compressibility  $\kappa^{-1}$  as a function of the inter-species scattering length  $a_{12}$  in the self-bound droplet regime. The solid red line is obtained using the MF+LHY functional, green squares and blue crosses are the predictions assuming POT-SR and POT-I functionals, respectively (see Table I and IV).

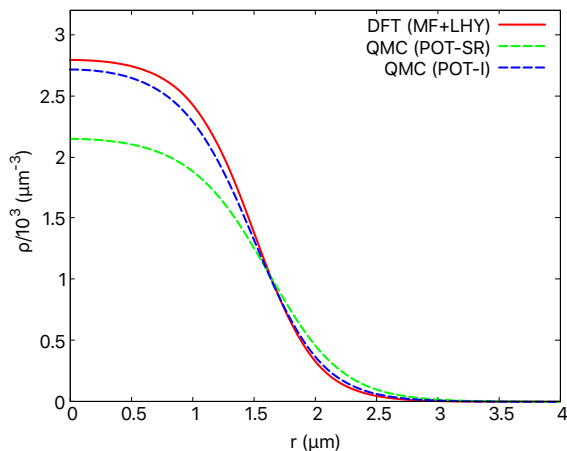


FIG. 7. Radial density profile for a droplet with  $a_{12} = -90 a_0$ : the prediction of MF+LHY (red solid line) are compared with the results obtained from a density functional reproducing the QMC results, either at zero-range (POT-SR, green dashed line) and with finite range effects (POT-I, blue dashed line).

In Fig. 6, the compressibility computed with the MF+LHY approach is shown for a set of values of the scattering length and compared to QMC results. In contrast to  $^{39}\text{K}$  droplets [16], the compressibility of QMC-based functional is higher compared to the MF+LHY, due to relatively smaller values of effective ranges in a K-Rb mixture.

Fig. 7 shows the calculated radial density profile for a droplet with  $a_{12} = -90 a_0$ , where a comparison is made between the prediction of the MF+LHY approach and those from the QMC-based energy functionals. The QMC-based functional, which relies on short-range model

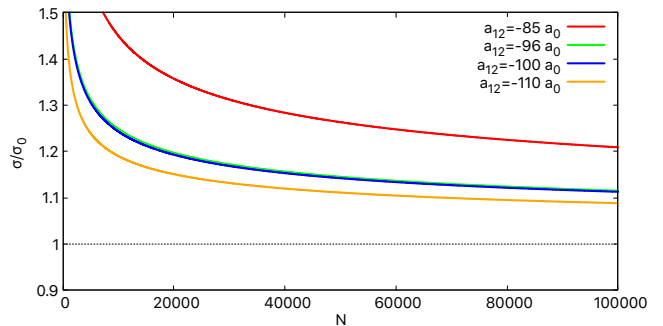


FIG. 8. Corrected and normalized surface tension  $\sigma/\sigma_0$  as a function of the total number of particles  $N$  in the droplet for a set of values of the inter-species scattering length  $a_{12}$ , computed within the MF+LHY framework.

potentials (POT-SR, see Fig. 1), predicts less dense droplets due to repulsive beyond-LHY energy contributions. Profiles obtained with the POT-I and MF+LHY functionals are more similar since the effect of increasing the effective range, included in POT-I through model potentials, is to increase binding energy and the peak density.

In Fig. 8, we show the dependence of the corrected surface tension  $\sigma$  as a function of the droplet's total number of particles  $N$ , computed within the MF+LHY framework by combining Eq. (28) with Eq. (25).

In Table V, we summarize the predictions for all observables analyzed in our work with the MF+LHY and QMC-based functionals for  $a_{12} = -85a_0$ ,  $-90a_0$  and  $-95a_0$ . It can be seen that QMC functionals show increasing deviation from the predictions of the MF+LHY functional as  $|a_{12}|$  increases. QMC-based density functionals constructed assuming short-range model potentials (POT-SR) predict larger deviations from the MF+LHY theory. When the correct effective range is included in the model potentials (POT-I), the predictions become more similar to those of MF+LHY. Variable most sensitive to beyond-LHY energy corrections appears to be the compressibility  $\kappa^{-1}$ , with a relative difference in the range  $\approx 20\%$  to  $130\%$ . This could have an impact on the collective excitation modes of a droplet [49], which will be investigated in a future study.

## VII. CONCLUSION

We have performed QMC calculations for the ground state of a K-Rb liquid mixture. We found that the zero-range model potentials used in a QMC calculation predict significant beyond LHY energy contributions. Otherwise, when the  $s$ -wave effective range is included in the model potentials, the energies fall close to the MF+LHY energies. Using both the MF+LHY and the QMC-based functionals, we have investigated funda-



TABLE V. Summary of all the quantities reported in the paper. Mass  $m$  is the mass of  $^{41}\text{Rb}$  atom, and  $a_0$  is Bohr radius.  $\epsilon_r(\text{POT-SR})$  and  $\epsilon_r(\text{POT-I})$  are the relative differences  $(O^{\text{POT-SR}} - O^{\text{MF+LHY}})/|O^{\text{MF+LHY}}|$  and  $(O^{\text{POT-I}} - O^{\text{MF+LHY}})/|O^{\text{MF+LHY}}|$  for observable  $O$ , given in percentages. Positive (negative) values of  $\epsilon_r$  mean that QMC functionals predict higher (lower) values of the observable with respect to MF+LHY one.

Observable	$a_{12}/a_0$	MF+LHY	POT-SR	POT-I	$\epsilon_r(\text{POT-SR})$	$\epsilon_r(\text{POT-I})$
$N_c$	-85	$2.07 \cdot 10^4$	$2.31 \cdot 10^4$	$2.26 \cdot 10^4$	12	9
	-90	$7.28 \cdot 10^3$	$8.47 \cdot 10^3$	$8.31 \cdot 10^3$	16	14
	-95	$3.49 \cdot 10^3$	$4.44 \cdot 10^3$	$4.10 \cdot 10^3$	27	17
$\frac{\sigma}{\hbar^2/(ma_0^4)}$	-85	$1.97 \cdot 10^{-20}$	$1.40 \cdot 10^{-20}$	$1.77 \cdot 10^{-20}$	-29	-10
	-90	$8.55 \cdot 10^{-20}$	$5.45 \cdot 10^{-20}$	$7.42 \cdot 10^{-20}$	-36	-13
	-95	$2.40 \cdot 10^{-19}$	$1.34 \cdot 10^{-19}$	$1.95 \cdot 10^{-19}$	-44	-19
$\Delta/a_0$	-85	$4.17 \cdot 10^4$	$4.78 \cdot 10^4$	$4.48 \cdot 10^4$	14	7
	-90	$2.23 \cdot 10^4$	$2.65 \cdot 10^4$	$2.46 \cdot 10^4$	19	11
	-95	$1.43 \cdot 10^4$	$1.80 \cdot 10^4$	$1.65 \cdot 10^4$	26	15
$\delta/a_0$	-85	$-5.53 \cdot 10^3$	$-6.57 \cdot 10^3$	$-6.16 \cdot 10^3$	-19	-11
	-90	$-2.95 \cdot 10^3$	$-3.67 \cdot 10^3$	$-3.43 \cdot 10^3$	-24	-16
	-95	$-1.90 \cdot 10^3$	$-2.50 \cdot 10^3$	$-2.35 \cdot 10^3$	-32	-24
$\frac{\kappa^{-1}}{ma_0^5/\hbar^2}$	-85	$2.81 \cdot 10^{23}$	$4.69 \cdot 10^{23}$	$3.47 \cdot 10^{23}$	67	24
	-90	$3.45 \cdot 10^{22}$	$6.73 \cdot 10^{22}$	$4.62 \cdot 10^{22}$	95	34
	-95	$7.90 \cdot 10^{21}$	$1.86 \cdot 10^{22}$	$1.20 \cdot 10^{22}$	135	52

mental surface properties for an experimentally relevant range of scattering parameters. These properties are relevant to the ongoing experiments because the observed droplets have a large surface-to-volume ratio. Upon entering a more correlated (denser) regime, the differences between the predictions for all quantities with the MF+LHY and the QMC-based functional grow.

## ACKNOWLEDGMENTS

This work has been supported by the Ministerio de Economía, Industria y Competitividad (MINECO,

Spain) under grants Nos. FIS2017-84114-C2-1-P and FIS2017-87801-P (AEI/FEDER, UE), and by the EC Research Innovation Action under the H2020 Programme, Project HPC-EUROPA3 (INFRAIA-2016-1-730897). V. C. gratefully acknowledges the computer resources and technical support provided by Barcelona Supercomputing Center. We also acknowledge financial support from Secretaria d'Universitats i Recerca del Departament d'Empresa i Coneixement de la Generalitat de Catalunya, co-funded by the European Union Regional Development Fund within the ERDF Operational Program of Catalunya (project QuantumCat, ref. 001-P-001644).

- 
- [1] D. S. Petrov, Quantum mechanical stabilization of a collapsing bose-bose mixture, *Phys. Rev. Lett.* **115**, 155302 (2015).
- [2] C. Cabrera, L. Tanzi, J. Sanz, B. Naylor, P. Thomas, P. Cheiney, and L. Tarruell, Quantum liquid droplets in a mixture of bose-einstein condensates, *Science* **359**, 301 (2018).
- [3] G. Semeghini, G. Ferioli, L. Masi, C. Mazzinghi, L. Wolswijk, F. Minardi, M. Modugno, G. Modugno, M. Inguscio, and M. Fattori, Self-bound quantum droplets of atomic mixtures in free space, *Phys. Rev. Lett.* **120**, 235301 (2018).
- [4] C. D'Errico, A. Burchianti, M. Prevedelli, L. Salasnich, F. Ancilotto, M. Modugno, F. Minardi, and C. Fort, Observation of quantum droplets in a heteronuclear bosonic mixture, *Phys. Rev. Research* **1**, 033155 (2019).
- [5] M. Barranco, R. Guardiola, S. Hernández, R. Mayol, J. Navarro, and M. Pi, Helium nanodroplets: An overview, *Journal of low temperature physics* **142**, 1 (2006).
- [6] F. Böttcher, M. Wenzel, J.-N. Schmidt, M. Guo, T. Langen, I. Ferrier-Barbut, T. Pfau, R. Bombín, J. Sánchez-Baena, J. Boronat, and F. Mazzanti, Dilute dipolar quantum droplets beyond the extended gross-pitaevskii equation, *Phys. Rev. Research* **1**, 033088 (2019).

- [7] L. Chomaz, S. Baier, D. Petter, M. J. Mark, F. Wächtler, L. Santos, and F. Ferlaino, Quantum-fluctuation-driven crossover from a dilute bose-einstein condensate to a macrodroplet in a dipolar quantum fluid, *Phys. Rev. X* **6**, 041039 (2016).
- [8] R. N. Bisset, L. A. P. Ardila, and L. Santos, Quantum droplets of dipolar mixtures, *Phys. Rev. Lett.* **126**, 025301 (2021).
- [9] C. J. Pethick and H. Smith, *Bose–Einstein condensation in dilute gases* (Cambridge university press, 2008).
- [10] T. D. Lee, K. Huang, and C. N. Yang, Eigenvalues and eigenfunctions of a bose system of hard spheres and its low-temperature properties, *Phys. Rev.* **106**, 1135 (1957).
- [11] D. M. Larsen, Binary mixtures of dilute bose gases with repulsive interactions at low temperature, *Annals of Physics* **24**, 89 (1963).
- [12] G. Ferioli, S. G., L. Masi, G. Giusti, G. Modugno, M. Inguscio, A. Gallemí, A. Recati, and M. Fattori, *Phys. Rev. Lett.* **122**, 090401 (2019).
- [13] V. Cikojević, L. V. Markić, M. Pi, M. Barranco, F. Ancilotto, and J. Boronat, Dynamics of equilibration and collisions in ultradilute quantum droplets (2021), arXiv:2104.09102 [cond-mat.quant-gas].
- [14] J. M. Escartín, F. Ancilotto, M. Barranco, and M. Pi, Vorticity and quantum turbulence in the merging of superfluid helium nanodroplets, *Physical Review B* **99**, 10.1103/physrevb.99.140505 (2019).
- [15] V. Cikojević, L. V. Markić, and J. Boronat, Finite-range effects in ultradilute quantum drops, *New Journal of Physics* **22**, 053045 (2020).
- [16] V. Cikojević, L. V. Markić, M. Pi, M. Barranco, and J. Boronat, Towards a quantum monte carlo-based density functional including finite-range effects: Excitation modes of a  $^{39}\text{K}$  quantum droplet, *Phys. Rev. A* **102**, 033335 (2020).
- [17] L. Parisi and S. Giorgini, Quantum droplets in one-dimensional bose mixtures: A quantum monte carlo study, *Phys. Rev. A* **102**, 023318 (2020).
- [18] D. S. Petrov and G. E. Astrakharchik, Ultradilute low-dimensional liquids, *Phys. Rev. Lett.* **117**, 100401 (2016).
- [19] M. Ota and G. E. Astrakharchik, Beyond Lee-Huang-Yang description of self-bound Bose mixtures, *SciPost Phys.* **9**, 20 (2020).
- [20] H. Hu and X.-J. Liu, Consistent theory of self-bound quantum droplets with bosonic pairing, *Phys. Rev. Lett.* **125**, 195302 (2020).
- [21] V. Cikojević, K. Dželalija, P. Stipanović, L. Vranješ Markić, and J. Boronat, Ultradilute quantum liquid drops, *Phys. Rev. B* **97**, 140502 (2018).
- [22] F. Ancilotto, M. Barranco, M. Guilleumas, and M. Pi, Self-bound ultradilute bose mixtures within local density approximation, *Phys. Rev. A* **98**, 053623 (2018).
- [23] F. Minardi, F. Ancilotto, A. Burchianti, C. D’Errico, C. Fort, and M. Modugno, Effective expression of the lee-huang-yang energy functional for heteronuclear mixtures, *Physical Review A* **100**, 063636 (2019).
- [24] C. Staudinger, F. Mazzanti, and R. E. Zillich, Self-bound bose mixtures, *Phys. Rev. A* **98**, 023633 (2018).
- [25] C. D’Errico, M. Zaccanti, M. Fattori, G. Roati, M. Inguscio, G. Modugno, and A. Simoni, Feshbach resonances in ultracold 39k, *New Journal of physics* **9**, 223 (2007).
- [26] A. Marte, T. Volz, J. Schuster, S. Dürr, G. Rempe, E. G. M. van Kempen, and B. J. Verhaar, Feshbach resonances in rubidium 87: Precision measurement and analysis, *Phys. Rev. Lett.* **89**, 283202 (2002).
- [27] V. Cikojević, L. V. Markić, G. E. Astrakharchik, and J. Boronat, Universality in ultradilute liquid bose-bose mixtures, *Phys. Rev. A* **99**, 023618 (2019).
- [28] A. Sarsa, J. Boronat, and J. Casulleras, Quadratic diffusion monte carlo and pure estimators for atoms, *The Journal of chemical physics* **116**, 5956 (2002).
- [29] J. Boronat, Microscopic approaches to quantum liquids in confined geometries, *World Scientific* , 21 (2002).
- [30] R. Jastrow, Many-body problem with strong forces, *Physical Review* **98**, 1479 (1955).
- [31] L. Reatto and G. Chester, Phonons and the properties of a bose system, *Physical Review* **155**, 88 (1967).
- [32] H. T. Stoof, K. B. Gubbels, and D. Dickerscheid, *Ultracold quantum fields* (Springer, 2009).
- [33] C. Chin, R. Grimm, P. Julienne, and E. Tiesinga, Feshbach resonances in ultracold gases, *Rev. Mod. Phys.* **82**, 1225 (2010).
- [34] G. F. Gribakin and V. V. Flambaum, Calculation of the scattering length in atomic collisions using the semiclassical approximation, *Phys. Rev. A* **48**, 546 (1993).
- [35] V. Flambaum, G. Gribakin, and C. Harabati, Analytical calculation of cold-atom scattering, *Phys. Rev. A* **59**, 1998 (1999).
- [36] L. M. Jensen, H. Nilsen, and G. Watanabe, Bcs-bec crossover in atomic fermi gases with a narrow resonance, *Physical Review A* **74**, 043608 (2006).
- [37] J. L. Bohn, J. P. Burke, C. H. Greene, H. Wang, P. L. Gould, and W. C. Stwalley, Collisional properties of ultracold potassium: Consequences for degenerate bose and fermi gases, *Phys. Rev. A* **59**, 3660 (1999).
- [38] G. Thalhammer, G. Barontini, J. Catani, F. Rabatti, C. Weber, A. Simoni, F. Minardi, and M. Inguscio, Collisional and molecular spectroscopy in an ultracold bose-bose mixture, *New Journal of Physics* **11**, 055044 (2009).
- [39] S. Stringari and J. Treiner, Surface properties of liquid  $^3\text{he}$  and  $^4\text{he}$ : A density-functional approach, *Phys. Rev. B* **36**, 8369 (1987).
- [40] R. C. Tolman, The effect of droplet size on surface tension, *The journal of chemical physics* **17**, 333 (1949).
- [41] E. Blokhuis and J. Kuipers, Thermodynamic expressions for the tolman length, *The Journal of chemical physics* **124**, 74701 (2006).
- [42] P. Rehner and J. Gross, Surface tension of droplets and tolman lengths of real substances and mixtures from density functional theory, *The Journal of Chemical Physics* **148**, 164703 (2018), <https://doi.org/10.1063/1.5020421>.
- [43] L. S. Bartell, Tolman’s  $\delta$ , surface curvature, compressibility effects, and the free energy of drops, *The Journal of Physical Chemistry B* **105**, 11615 (2001).
- [44] S. Mayer, A molecular parameter relationship between surface tension and liquid compressibility, *The Journal of Physical Chemistry* **67**, 2160 (1963).
- [45] W. Helfrich, Elastic properties of lipid bilayers: theory and possible experiments, *Zeitschrift für Naturforschung C* **28**, 693 (1973).
- [46] S. Fisk and B. Widom, Structure and free energy of the interface between fluid phases in equilibrium near the critical point, *The Journal of Chemical Physics* **50**, 3219 (1969).
- [47] P. Egelstaff and B. Widom, Liquid surface tension near the triple point, *The Journal of Chemical Physics* **53**, 2667 (1970).

- [48] K. Mon and D. Stroud, Surface widths of simple liquids and an empirical law of freezing, *The Journal of Chemical Physics* **74**, 2078 (1981).
- [49] H. Hu and X.-J. Liu, Collective excitations of a spherical ultradilute quantum droplet, *Phys. Rev. A* **102**, 053303 (2020).